

Article

Construction of a Numerical Model for Flow Flash Evaporation with Non-Condensable Gas

Wei Wang *, **Bingrui Li**, **Xin Wang**, **Bingxi Li** and **Yong Shuai**

School of Energy Science and Engineering, Harbin Institute of Technology, Harbin 150001, China;
libingrui@stu.hit.edu.cn (B.L.); 23s102138@stu.hit.edu.cn (X.W.); libx@hit.edu.cn (B.L.);
shuaiyong@hit.edu.cn (Y.S.)

* Correspondence: wangwei36@hit.edu.cn

Abstract: Flash evaporation processes are widely used in petroleum, food, chemical, power, and other industries to separate products or extract heat. The liquid is often entrained by non-condensing gas components. This study develops a multiphase, multicomponent, and pressure-driven phase-change-coupled model to numerically study water flash evaporation with non-condensing CO₂. The model includes the mass, momentum, energy, volume of fluid (VOF), species transport, turbulence (RNG k-ε), modified phase-change Lee, and non-condensing CO₂ release governing equations. The steam generation rate and mechanism for pure water and different concentrations of CO₂ are considered. The results show that the numerical model can accurately predict the flash evaporation process and has high accuracy compared with the experimental data. Both the dissolved and entrained CO₂ that are released can severely disturb the flow field, leading to an increase in the steam generation rate. Under a 1–10% volume concentration of dissolved CO₂ and 0.0661–0.1688% mass concentration of entrained CO₂, the maximum increase ratio of steam generation can reach 20%.

Keywords: flash evaporation; non-condensing gas; numerical investigation; heat and mass transfer; steam generation rate



Citation: Wang, W.; Li, B.; Wang, X.; Li, B.; Shuai, Y. Construction of a Numerical Model for Flow Flash Evaporation with Non-Condensable Gas. *Appl. Sci.* **2023**, *13*, 11638. <https://doi.org/10.3390/app132111638>

Academic Editor: Francesca Scargiali

Received: 25 September 2023

Revised: 15 October 2023

Accepted: 20 October 2023

Published: 24 October 2023



Copyright: © 2023 by the authors. Licensee MDPI, Basel, Switzerland. This article is an open access article distributed under the terms and conditions of the Creative Commons Attribution (CC BY) license (<https://creativecommons.org/licenses/by/4.0/>).

1. Introduction

Low-pressure flash evaporation is a unique evaporation technique that is different from evaporation from an overheated surface. Steam is primarily produced at the liquid surface because ambient atmospheric pressure is lower than the saturation pressure of the temperature of the liquid [1]. This technique offers a high evaporation rate without requiring excessively high liquid temperatures. Flash evaporation is widely used in many industrial fields, such as seawater desalination, chemical engineering, food processing, ocean thermal energy conversion, and waste heat recovery [2,3].

Many factors have a significant effect on the flash evaporation rate, such as the liquid temperature, atmospheric pressure, saturation pressure, initial liquid height, and liquid flow rate [4]. Several experimental studies have been conducted on this topic. Wu et al. [5] experimentally studied flash evaporation under low-pressure conditions, with the water temperature ranging from 50.0 to 90.5 °C, initial water height of 400 mm to 550 mm, and superheats ranging from 1.5 K to 17.8 K; the results showed that an increase in water temperature and a decrease in the initial liquid level height can enhance the extent of flash evaporation. Zhang et al. [6] studied water flash evaporation with different values of flow rate (400–1200 L h⁻¹), water film concentration (0–10%), and pressure (7.4–47.4 kPa). Ni et al. [7] experimentally investigated the effect of different sealing air flows on the flash evaporation rate. The valve opening ratio varied from 0.125 to 1. Chi et al. [8] experimentally studied the thermal characteristics of water flash evaporation from a thin liquid film. The experimental operating conditions were an initial temperature in the range of 60–85 °C, a liquid film height of 3–20 mm, and a superheat in the range of 2–22 K. Lior and Nishiyama [9] experimentally investigated the use of electrolytically generated hydrogen bubbles to improve flash evaporation performance. They found that

hydrogen bubbles promoted ebullition in the regions of the flash stage, and thus reduced the non-equilibrium temperature difference by up to 15%. Tian et al. [10] investigated water flash evaporation under a microwave. The temperature ranged from 19 to 50 °C, pressure from 4–12 kPa, flow rate from 10–40 L h⁻¹, and the microwave power ranged from 0.81 to 1.35 kW. Wang et al. [11] conducted experimental and theoretical studies on water flash evaporation and developed a one-dimensional (1D) mathematical model. The model considered four main physical processes: gas outflow due to depressurization, mild evaporation, flash evaporation, and the updated flashing chamber pressure and gas components. Zhang et al. [12] experimentally studied the static flash evaporation of aqueous NaCl solutions at flash speeds in the range of 4.8×10^{-4} –2.18 s⁻¹.

While many experimental studies have explored some physical regulations, there still remain gaps in the understanding. However, owing to the limitations of experimental test methods, our understanding of the internal heat and mass transfer mechanisms remains unclear. In addition, experimental tests are time consuming and costly, and it is difficult to reproduce the experimental results in other working conditions. Similarly, there are problems of errors and assumptions in the calculations and numerical model, making the simulation not always completely accurate, but with the development of computers, numerical methods have attracted increasing attention. Xie et al. [13] used the volume of fluid (VOF) and Lee models to simulate the flash point of ethylene glycol. The results showed that the flash point varied at different measurement points, and a lower flash point could be obtained at the measurement point with a higher vapor volume fraction. The vapor volume fraction and temperature showed strong fluctuations, and the measurement deviations of the flash points were closely related to the fluctuations of the vapor temperature. A mathematical model was developed by Cheng et al. [14] to numerically simulate the droplet and film flash evaporation. The results showed that droplet flash evaporation significantly affected the cooling heat transfer of vacuum flash evaporation. Gao et al. [15] proposed a mathematical model to predict the flash evaporation of LiCl droplets released into a vacuum. They found that the pressure is the core factor affecting the evaporation rate, i.e., the lower the pressure, the more intense the flash. Droplets with a higher initial temperature only strengthened the intensity of flash evaporation at the beginning. The model can accurately predict droplet flash evaporation without radiation heat. Ji et al. [16] conducted a three-dimensional (3D) simulation of the flash evaporation of a non-uniform spray in a saturated vapor environment using the Eulerian–Lagrangian framework in the software Fluent. The spray initially underwent violent evaporation and a significant temperature reduction within the vicinity of the nozzle exit. As the spray develops downstream, evaporation becomes moderate. Smaller droplets were distributed in the central spray region, with a comparatively higher evaporation rate and larger velocity variation. Jin and Low [17] used a single-phase model to study the flow-field distribution in a flash evaporation chamber. Wang et al. [18] established a 1D droplet flash evaporation model by introducing a simple heat balance correlation and a phase-transition model to Fick's law. The effects of ambient pressure, temperature, droplet size, and the fraction of vapor concentration on the flash evaporation and spray cooling rate were presented in detail.

The presence of non-condensable gases in the vapor can have a serious effect on the heat transfer process in the condenser, as it reduces the partial pressure of the vapor around the cooling surface and increases the transfer resistance of the vapor to the cooling surface, which ultimately leads to a reduction in the amount of heat transferred and an increase in the vacuum load of the condensing system. Many scholars have studied the effects of non-condensable gas. Drożyński [19] studied the significant influence of non-condensable gases on the steam condensation process; in particular, the presence of non-condensable gases increases the pressure in the equipment and affects the condensation efficiency. Balaji et al. [20] investigated the effect of non-condensable gases in a low-temperature thermal desalination system and showed that each unit mass of non-condensable gas flowing into the condensation chamber resulted in 1.6 times the unit vapor loss from the vacuum pump outlet. Gentner et al. [21] studied the effect of non-condensable gases in

multiple-effect distillation systems and showed that the presence of non-condensable gases increased the heat transfer area of a horizontal tube condenser by about 10–30%, while each unit of non-condensable gases led to a loss of 20–30 units of vapor under severe operating conditions.

The aforementioned numerical studies all treated liquid as a single phase. However, in the industry, liquids often include and dissolve a significant amount of non-condensing gases. Therefore, we propose a new coupled numerical model that includes multiphase, multicomponent, phase-change, and turbulent-flow modules that can accurately predict the liquid flash evaporation process with a non-condensing gas. The non-condensing gas was considered to be dissolved and entrained into two components in the liquid. The effects of the two types of non-condensing gases on the flash evaporation mechanism and steam generation rates are discussed in detail.

2. Construction of the Numerical Model

2.1. Physical Model and Boundary Conditions

A horizontal-flow flash chamber with three openings, namely, the fluid inlet, fluid outlet, and steam outlet, was studied, as shown in Figure 1a. The chamber length and width were 1 m and 1.4 m, respectively. A structured grid was used in the chamber, as shown in Figure 1b. Four grid sizes were independently tested, and the grid sizes were 3.0, 2.5, 2.0, and 1.5 mm, corresponding to 154,845, 224,000, 350,000, and 620,712 grids, respectively. A grid size of 2.0 mm was selected because of the computational time and clarity of the results.

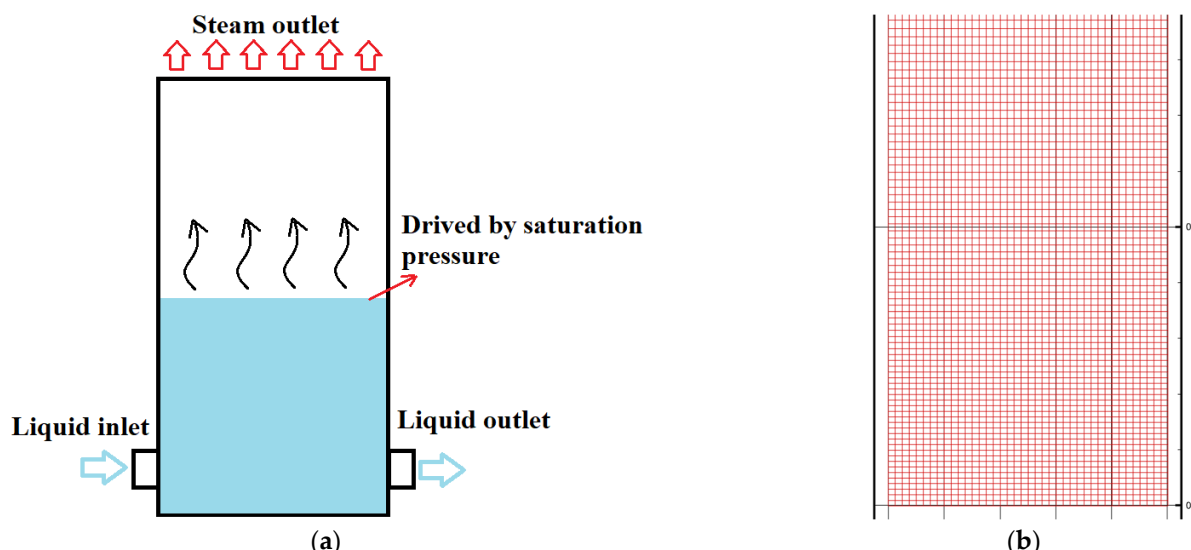


Figure 1. Computational domain and grid structure of the flash chamber: (a) computational domain; (b) grid structure.

2.2. Working Conditions and Boundary Conditions

This study investigated water flow with non-condensable CO_2 . Two types of non-condensable CO_2 were considered, namely, the dissolved and entrained components in water [22,23], and were respectively considered as liquid-phase $\text{CO}_{2(\text{aq})}$ and gas-phase $\text{CO}_{2(\text{g})}$. Before flash evaporation, the water in the flash chamber had an initial water-level height (h) controlled by the static pressure of the liquid outlet ($P_{\text{out},l}$). During the working process, the environmental pressure of the flash chamber (controlled by the pressure of the vapor outlet $P_{\text{out},v}$) was lower than the saturation pressure corresponding to the inlet temperature (T_{in}), and the pressure difference was the driving force of the flash process.

The inlet conditions were water with a fixed temperature (T_{in}) and mass flow rate. Different masses of carbon dioxide entered the flash chamber together as a gas or solute

in water, depending on the operating conditions. The vapor and liquid outlets are both pressure conditions, where the steam outlet ($P_{out,v}$) pressure is equal to 19.9 kPa, and the liquid outlet pressure is equal to 19.9 kPa at the water-height pressure (ρgh). The physical parameters of water and vapor at different temperatures are listed in Table 1. The physical properties of water were assumed to have fixed values corresponding to $P_{out,v}$, and the vapor was assumed to be an ideal gas for calculating its density under different temperatures and pressures.

Table 1. Physical properties of saturated water and saturated steam at 19.9 kPa.

Materials	ρ	c_p	λ	μ
water	983.16	4185.1	0.65100	0.00046602
vapor	—	1964.8	0.02104	0.00001085

2.3. Model Construction and Governing Equations

In this study, a multiphase, multicomponent, and pressure-driven Lee phase-change-coupled model was proposed [24]. The governing equations and calculation flowchart are shown in Figure 2. The left side of the chart shows the main governing equations, including the transient momentum conservation equations, mass conservation equation, energy conservation equation, phase fraction conservation equation (VOF model), and the non-condensing gas fraction equation. The right side shows the calculated equations for the phase change and released non-condensing CO₂ source term, which is the original model of this work. The phase-change ratio in the conventional Lee model is calculated using the temperature difference ($T-T_{sat}$), whereas in this study, T_{sat} is not a fixed value and is calculated using the local pressure, as shown in Equations (18) and (19). Two types of dissolved components are released (CO_{2(aq)}): supersaturation release and interfacial diffusion release, corresponding to Equations (20) and (23), respectively.

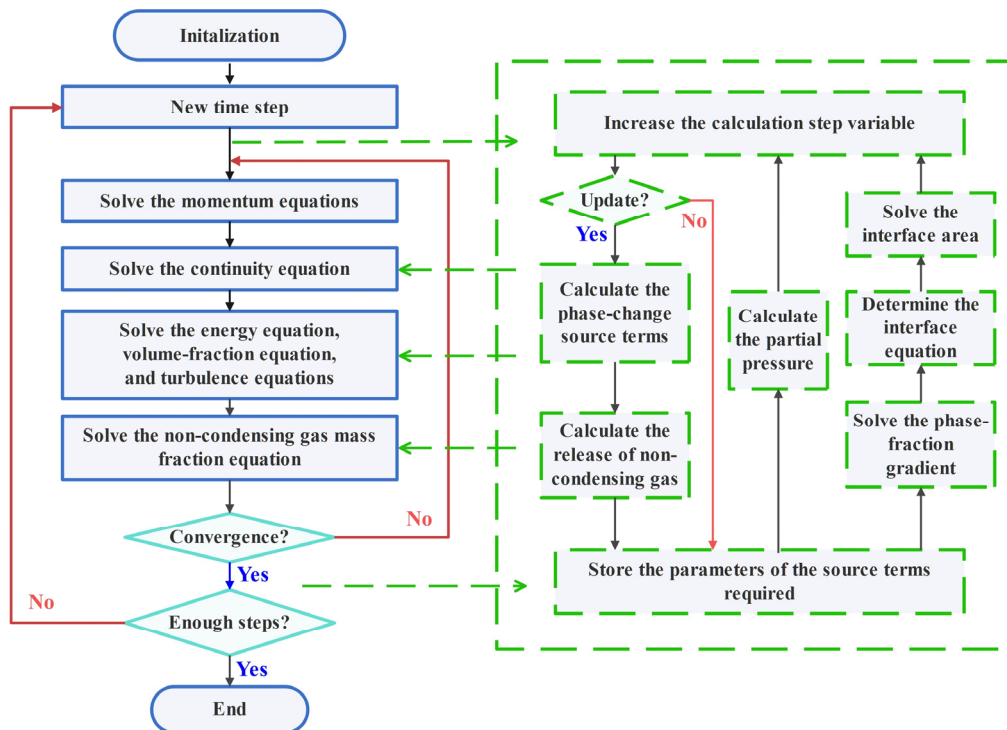


Figure 2. Flow chart of the numerical model calculation.

2.3.1. Mass, Momentum, and Energy Equations

Equations (1)–(3) show the conservation of mass, momentum, and energy of the two phases, respectively. The calculated pressure, velocity, and temperature are shared between the two phases, and the relative motion of the two phases can be described by variations in the local phase fraction [25,26].

$$\frac{\partial \rho}{\partial t} + \nabla \cdot \rho v = 0 \quad (1)$$

$$\frac{\partial}{\partial t}(\rho v) + \nabla \cdot (\rho v v) = -\nabla p + \nabla \cdot \mu(\nabla v) + \rho g + F_{\text{CSF}} \quad (2)$$

$$\frac{\partial}{\partial t}(\rho E) + \nabla \cdot [(\rho E + p)v] = \nabla \cdot (\lambda \nabla T) + \dot{S}_{\text{lv}} \quad (3)$$

where t represents time, p is the local pressure, v is the local velocity vector, ρ is the density of the mixture, μ is the dynamic viscosity, λ is the thermal conductivity, T is the local temperature, g is the gravitational acceleration vector, E is the internal energy, and \dot{S}_{lv} is the source term of energy.

The density of the vapor is calculated using the ideal gas equation of state, which is updated before each calculation step, as shown in Equation (4), where M_W is the molar mass of water, taken as $0.018 \text{ kg mol}^{-1}$, and R is the ideal gas constant of $8.314 \text{ J}/(\text{mol}\cdot\text{K})$.

$$\rho_v = p M_W / RT \quad (4)$$

The F_{CSF} is the source term of the volume force used to characterize the surface tension, as shown in Equations (5) and (6). Its representation was derived from a continuum surface force model [27]. The model assumes that the surface tension is constant along the surface and models only the normal force. The magnitude of the pressure drop across the surface is obtained from the magnitude of the curvature of the interface κ and the surface tension coefficient σ , and the calculation is added in the form of the source term of the momentum equation by deriving the divergence theorem.

$$F_{\text{CSF}} = \sigma \frac{\rho \kappa \nabla \alpha}{0.5(\rho_1 + \rho_v)} \quad (5)$$

$$\kappa = \nabla \cdot \frac{\nabla \alpha}{|\nabla \alpha|} \quad (6)$$

2.3.2. VOF Equations

By solving the partial differential equation of the phase fraction, the VOF method can obtain the percentage of each phase in different cells and show the overall gas–liquid distribution. The volume-fraction equation of the VOF model is expressed as follows [28]:

$$\frac{\partial \alpha_l \rho_l}{\partial t} + \nabla \cdot (\alpha_l \rho_l v) = -\dot{m}_{\text{lv}} \quad (7)$$

where α_l is the volume fraction of the liquid phase, and \dot{m}_{lv} is the rate of transfer of mass in units of $\text{kg}/(\text{m}^3 \text{ s})$. During the calculations, α_l is kept in the range of 0 to 1, and the volume fraction of the gas phase and liquid phase must sum to 1 in a finite volume, which provides the distribution of the liquid and gas phases within a single cell.

Furthermore, the magnitude of the internal energy of the unit that mixed the two phases in the energy equation was calculated using the following equation:

$$E = \frac{\alpha_l \rho_l E_l + \alpha_v \rho_v E_v}{\alpha_l \rho_l + \alpha_v \rho_v} \quad (8)$$

$$E_i = c_{p,i}(T - 273.15\text{K}) \quad (9)$$

where μ , ρ , and λ are the dynamic viscosity, density, and thermal conductivity of the mixture, respectively. These physical properties Φ can be calculated by averaging the volume fraction as shown below [29].

$$\Phi = \Phi_l \alpha_l + \Phi_v \alpha_v \quad (10)$$

2.3.3. Species Transport Equations

The dissolved $\text{CO}_{2(\text{aq})}$ and entrained $\text{CO}_{2(\text{g})}$ in the water were released and dispersed in the flash chamber. To describe the distribution of CO_2 within the flash chamber, component mass fraction equations were added as shown in the following equations [30]:

$$\frac{\partial}{\partial t} (\rho_l \alpha_l Y_{\text{CO}_{2(\text{aq})}}) + \nabla \cdot (\rho_l \alpha_l v Y_{\text{CO}_{2(\text{aq})}}) = -\nabla \cdot (\alpha_l J_{\text{CO}_{2(\text{aq})}}) - \dot{m}_{\text{CO}_2} \quad (11)$$

$$\frac{\partial}{\partial t} (\rho_v \alpha_v Y_{\text{CO}_{2(\text{g})}}) + \nabla \cdot (\rho_v \alpha_v v Y_{\text{CO}_{2(\text{g})}}) = -\nabla \cdot (\alpha_v J_{\text{CO}_{2(\text{g})}}) + \dot{m}_{\text{CO}_2} \quad (12)$$

In the above equations, $Y_{\text{CO}_{2(\text{aq})}}$ and $Y_{\text{CO}_{2(\text{g})}}$ are the mass fractions of CO_2 in the form of solute in water and gas in vapor, respectively. The left side shows the unsteady-state terms and convection terms of the mass fraction, and the right side shows the diffusion terms and interphase transfer source terms, where the source terms are used to characterize the variation in CO_2 during the release of dissolved gases. In the turbulent state, the diffusion flux J_i can be expressed using the following formula:

$$J_i = -(\rho D_{ij} + \frac{\mu_t}{Sc_t}) \nabla Y_i - D_{T,i} \frac{\nabla T}{T} \quad (13)$$

In this formula, the first term on the right side is the diffusion flux that is obtained based on Fick's law, which includes the diffusion caused by both the concentration gradient and turbulence. μ_t is the turbulent viscosity, $D_{T,i}$ is the thermal mass diffusion coefficient, and Sc_t is the turbulent Schmidt number, which is equal to 0.7. In this numerical model, the diffusion coefficient D_{ij} of CO_2 in water was taken as $4.1 \times 10^{-9} \text{ m}^2 \text{ s}^{-1}$ [31], and the diffusion coefficient D_{ij} of CO_2 in vapor was taken as $0.26 \times 10^{-4} \text{ m}^2 \text{ s}^{-1}$ [32].

2.3.4. Turbulence Equations

In addition, the RNG $k-\varepsilon$ model was selected to simulate the turbulent flow in the flash tank. This model has a better result of turbulence simulation compared to the Standard $k-\varepsilon$ and RSM models in the VOF model for stratified flow simulation [33,34]. This model calculates the turbulent kinetic energy in the flow by solving the k and ε equations. The control equations are shown in Equations (14) and (15).

$$\frac{\partial(\rho k)}{\partial t} + \frac{\partial(\rho k u_i)}{\partial x_i} = \frac{\partial}{\partial x_j} (1.393 \mu_{\text{eff}} \frac{\partial k}{\partial x_j}) + G_k + \rho \varepsilon \quad (14)$$

$$\frac{\partial(\rho \varepsilon)}{\partial t} + \frac{\partial(\rho \varepsilon u_i)}{\partial x_i} = \frac{\partial}{\partial x_j} (1.393 \mu_{\text{eff}} \frac{\partial \varepsilon}{\partial x_j}) + \frac{C_{1\varepsilon}^* \varepsilon}{k} G_k - 1.68 \rho \frac{\varepsilon^2}{k} \quad (15)$$

where k represents the turbulent kinetic energy, ε represents the turbulent dissipation rate, G_k represents the generation of turbulence kinetic energy due to the mean velocity gradients, and μ_{eff} is the corrected turbulence viscosity.

2.3.5. Phase-Change Lee Equations

Based on the above model, the values of the source terms \dot{m}_{lv} and \dot{S}_{lv} in Equations (3) and (7) were further varied to simulate the phase-change process.

The transfer of water from the liquid phase to the gas phase during the phase-change process is described by \dot{m}_{lv} in the volume-fraction equation, which ultimately leads to a decrease in α_l and an increase in α_v . The decrease in sensible heat owing to evaporation is controlled by the energy source term \dot{S}_{lv} in the energy equation.

In this case, the values of the source terms were obtained from the modified Lee model, as shown in Equations (16) and (17).

$$\dot{m}_{lv} = \begin{cases} c \times \frac{\alpha_l \rho_l (T - 31.35 p_w^{0.1526} + 191.1)}{31.35 p_w^{0.1526} + 191.1} & (T_l > 31.35 p_w^{0.1526} + 191.1) \\ 0 & (T_l \leq 31.35 p_w^{0.1526} + 191.1) \end{cases} \quad (16)$$

$$\dot{S}_{lv} = -\dot{m}_{lv} r \quad (17)$$

where c represents the time relaxation parameter, p_w is the partial pressure of local water, and r is the latent heat of evaporation.

As shown in the two equations above, this model first determines whether the cell is undergoing a phase transition, and it then calculates the source terms of the phase-transition cell using the local temperature and static pressure. This approach does not require a distinction between nucleation boiling and interfacial mass transfer and uses the same operation to deal with the boiling phenomenon that occurs in both the phase-interface cell and the cells filled with liquid, which leads to a simple and effective simulation of the full-scale flow boiling phenomenon.

Compared to the original Lee model, the main change in the previously described model is that the driving force of the source term is provided by the local pressure and temperature. This modification is important because a small local pressure change at low ambient pressures can have a significant impact on the saturation temperature in that the distribution of water pressure due to gravity can lead to a non-uniform distribution of the flash vapor rate.

2.3.6. Non-Condensing CO₂ Release Model

The release process was divided into two modes, supersaturated precipitation (\dot{S}_i) and interfacial diffusion (\dot{S}_s), as follows:

$$\dot{m}_{CO_2} = \dot{m}_s + \dot{m}_{id} \quad (18)$$

The supersaturated release rate (\dot{m}_s) is caused by the supersaturated solubility, which occurs when the mass fraction of CO₂ in the local liquid phase is greater than the corresponding solubility of the local pressure. This is calculated as follows:

$$\dot{m}_s = c_s \rho_l \alpha_l (Y_{CO_2(aq)} - \frac{p_{CO_2}}{k_H}) \quad (19)$$

where c_s is the supersaturation release coefficient, $Y_{CO_2(aq)}$ is the dissolved gas mass fraction for a single grid, Henry's constant for carbon dioxide dissolved in water k_H is 6×10^7 pa [35], and p_{CO_2} is the CO₂ partial pressure obtained using Dalton's law as follows:

$$p_w = p \times \frac{(1 - Y_{CO_2(g)})/18}{Y_{CO_2(g)}/44 + (1 - Y_{CO_2(g)})/18} \quad (20)$$

$$p_{CO_2} = p \times \frac{Y_{CO_2(g)}/44}{Y_{CO_2(g)}/44 + (1 - Y_{CO_2(g)})/18} \quad (21)$$

The interfacial diffusion (\dot{m}_{id}) of CO₂ is caused by the gas–liquid concentration difference at the interface. The process was activated when the local liquid-phase CO₂ concentration exceeded the local gas-phase CO₂ concentration as follows:

$$\dot{m}_{\text{id}} = c_{\text{id}} A (\rho_l Y_{\text{CO}_2(\text{aq})} - \rho_v Y_{\text{CO}_2(\text{g})}) \quad (22)$$

where c_{i} is the interface release coefficient, and A is the interface area. In this study, a simple geometric reconstruction method is employed to obtain the interface area. For a single grid, only the phase fraction and gradient were considered, and the continuity of the interface was ignored. Four typical gas–liquid distribution types in a single grid are illustrated in Figure 3.

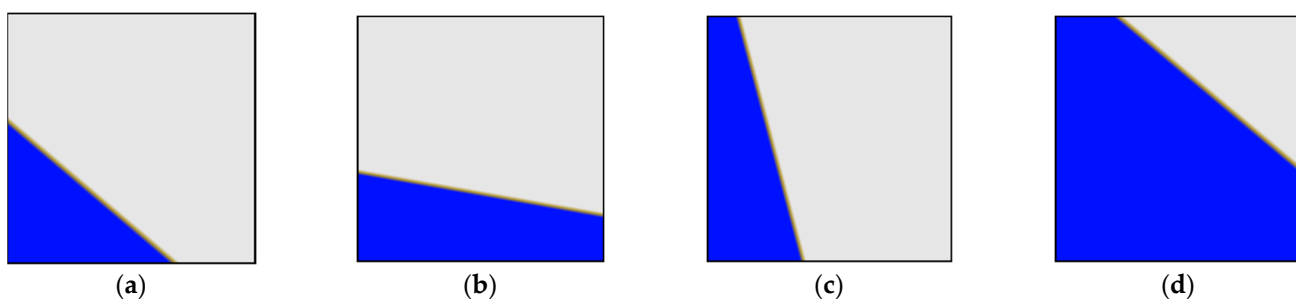


Figure 3. Four typical gas–liquid distribution types in a single grid: (a) $C_x < X_{\text{cell}}$, $C_y < Y_{\text{cell}}$; (b) $C_x > X_{\text{cell}}$, $C_y < Y_{\text{cell}}$; (c) $C_x < X_{\text{cell}}$, $C_y > Y_{\text{cell}}$; (d) $C_x > X_{\text{cell}}$, $C_y > Y_{\text{cell}}$.

For the four interfacial types, the specific solution processes of the interface area are as follows: (1) the position of the main body of the liquid phase is obtained by the positive and negative values of the gradient components of the phase fraction, and the coordinate system is established with the grid corner of the main body of the liquid phase as the origin; (2) the normal vector and slope of the interface are obtained by the phase fractional gradient; (3) the interface linear equation intercept is calculated using the phase fraction; and (4) finally, the linear equations of the phase interface and the grid intersection are obtained, and the interface area is solved using the Equation (23).

$$\begin{cases} A = |\nabla \alpha_v| \sqrt{2X_{\text{cell}}Y_{\text{cell}}\alpha_v / |\nabla \alpha_{v,x}| |\nabla \alpha_{v,y}|} & (C_x > X_{\text{cell}}, C_y > Y_{\text{cell}}) \\ A = |\nabla \alpha_v| X_{\text{cell}} / |\nabla \alpha_{v,y}| & (C_x > X_{\text{cell}}, C_y < Y_{\text{cell}}) \\ A = |\nabla \alpha_v| Y_{\text{cell}} / |\nabla \alpha_{v,x}| & (C_x < X_{\text{cell}}, C_y > Y_{\text{cell}}) \\ A = |\nabla \alpha_v| \sqrt{2X_{\text{cell}}Y_{\text{cell}}\alpha_v / |\nabla \alpha_{v,x}| |\nabla \alpha_{v,y}|} & (C_x < X_{\text{cell}}, C_y < Y_{\text{cell}}) \end{cases} \quad (23)$$

where X_{cell} and Y_{cell} represent the width of the local grid in the x and y directions, respectively, $\nabla \alpha_{v,x}$ and $\nabla \alpha_{v,y}$ are the local grid liquid fraction gradients in the x and y directions, respectively, and C_x and C_y are the intersection points of the interface line with the x -axis and y -axis, respectively.

2.4. Numerical Method

The PISO method was used to couple the momentum and mass equations. The gradient was obtained using the least-squares method, and the density, momentum, turbulent kinetic energy, turbulent dissipation rate, and energy equations were in a first-order windward discrete format. The time step used for transient calculations was 5×10^{-5} s. The under-relaxation factors were used at values 0.3 (pressure), 0.3 (momentum), 0.5 (turbulent kinetic energy and turbulent dissipation rate), 1 (mass fraction), and 0.8 (energy) [36,37]. The convergence criterion was set to a residual of less than 10^{-6} (energy equation) and 10^{-3} (continuity, momentum, turbulence, and CO₂ transport equations).

In addition, Ding et al. [38] showed that numerical oscillations may occur when using the Lee model for phase-transition processes, especially in the presence of excessively large evaporation coefficients. To ensure that the calculation had better stability, this study assumed that the local pressure did not change within 1 ms. This assumption effectively increases the convergence of the calculations.

3. Results and Discussion

3.1. Model Verification

The results obtained from the numerical model constructed in this study were compared with experimental data [39], and the release rates (c_s and c_{id}) were determined based on the experimental data. The experimental test shown in Figure 4a illustrates a cylindrical vessel with an inner diameter of 0.045 m, a height of 0.2 m, and a water height of 0.15 m. The experimental operation used dissolved saturated CO₂ water from 5.4 bar decreasing to three pressure cases (5.31, 5.23, and 5.08 bar). The experimental release rate at 100 s was selected and compared with the numerical results, as shown in Figure 4b, and the maximum error was less than $\pm 10\%$. The release coefficients of supersaturation CO₂ (c_s) and interface diffusion CO₂ (c_{id}) were 8.8×10^{-6} (1/s) and 0.01 (1/m²·s), respectively.

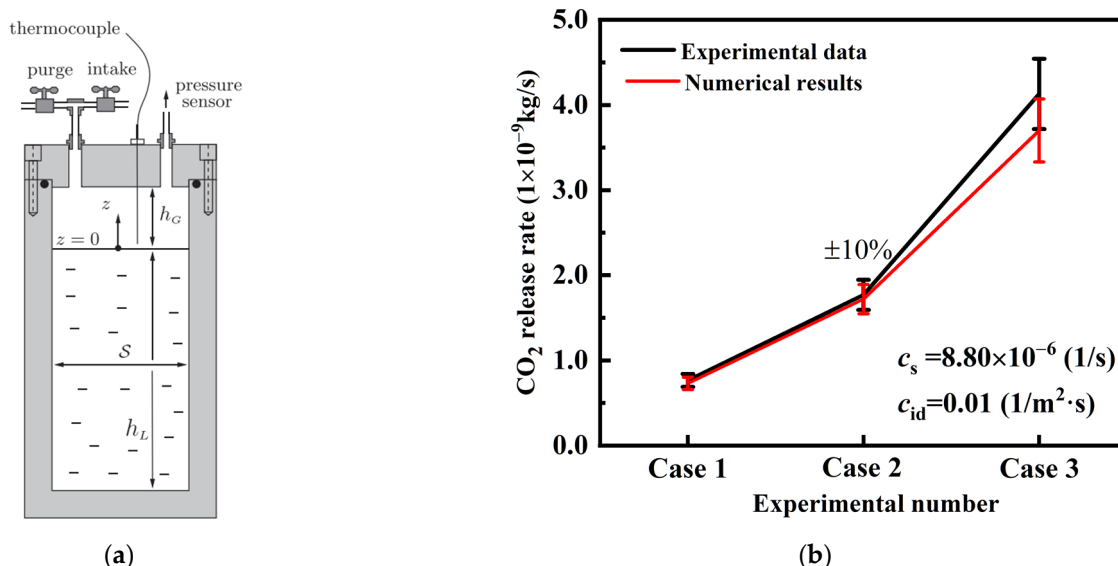


Figure 4. Validation of the numerical model with experimental CO₂ release rate data: (a) schematic diagram of the experimental model Re-printed with permission from Ref. [39]. 2014, Elsevier Inc.; (b) comparison of the experimental and numerical results.

In addition, the flash evaporation process without the presence of non-condensable gases was also compared with the experimental results [40]. The flash chamber for the flow flash evaporation used in the experimental articles compared had an internal flash space of 480 mm in height, 100 mm in length, and 100 mm in width. Five sets of numerical simulation experiments with different inlet temperatures were carried out under the conditions of an initial water-level height of 120 mm and flow rate of 800 L/h. The comparison results are shown in Figure 5 below, and the steam generation rate obtained from the numerical simulation shows a good accuracy.

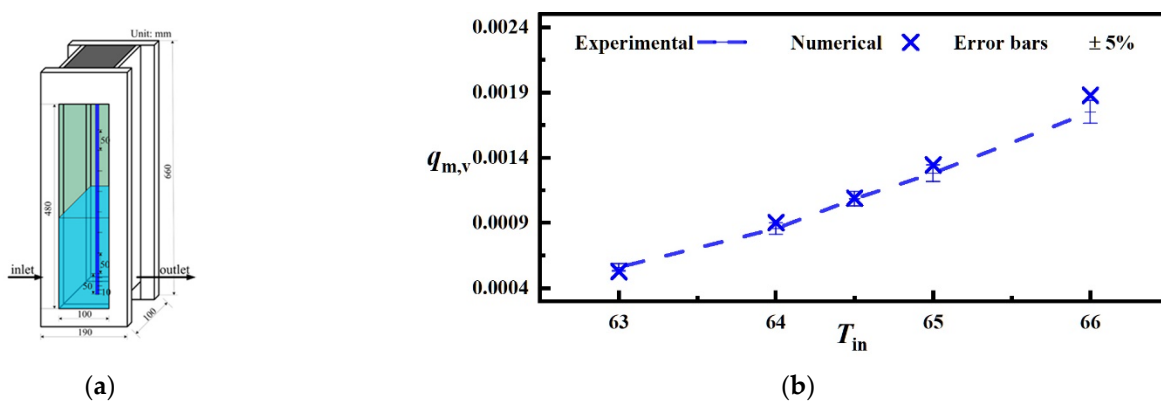


Figure 5. Validation of the numerical model with experimental CO_2 release rate data: (a) schematic diagram of the experimental model Re-adapted with permission from Ref. [40]. 2013, Elsevier Ltd.; (b) comparison of the experimental and numerical results.

3.2. Effect of Entrained CO_2 Concentration on Flash Performance

The 63.5 °C water with four kinds of entrained CO_2 volume concentrations (1 vol%, 4 vol%, 7 vol%, and 10 vol%) was compared. The steam generation rate and CO_2 release rate after flash process stabilization are shown in Figure 6. Compared with pure water, the steam generation rate for water with entrained CO_2 increased by approximately 4.8%, 11.7%, 15.9%, and 20.0%, corresponding to volumes of 1%, 4%, 7%, and 10%, respectively. The increase in the steam generation rate is proportional to the increase in the steam-carrying volume. Compared with pure water, the presence of entrained CO_2 leads to an increase in the steam evaporation rate per step. In addition, the percentage of CO_2 components in the outlet steam of the flash chamber increased significantly with the inlet flow of entrained CO_2 and were approximately 0.13%, 0.50%, 0.84%, and 1.16%, respectively.

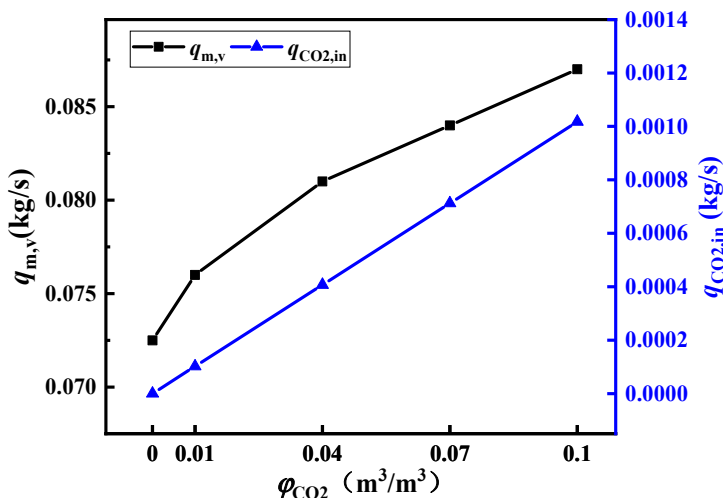


Figure 6. Variation in the steam generation rate and CO_2 release rate of different entrained CO_2 volume fractions.

The temperature, phase, CO_2 concentration, partial pressure, absolute pressure, and local steam production rate distribution are shown in Figure 7, under the 1 vol% entrained CO_2 volume concentration. As shown in Figure 7a, there is an area of high temperature above the inlet area, which is caused by non-condensable gas. Under the effect of gravity, the CO_2 entrained in the inlet water quickly floats upwards after entering the flash chamber and rapidly drives the water upwards, leading to an increase in water temperature above the inlet region. As can be seen from the distribution of local vapor generation rates in Figure 7, the regions of intense phase change include the low-pressure region at the top and

the region near the inlet where carbon dioxide is present in large quantities. The increase in the flash steam generation rate was caused primarily by the high temperature and low water vapor partial pressure around the entrance of the flash chamber. The entrained CO₂ gas in the flash chamber had little effect on the total pressure stratification phenomenon of the flash tank; however, the local high CO₂ concentration reduced the partial pressure of the steam in the air space near the inlet. Under the combined effect of the low partial pressure of steam and the high temperature at the inlet, there was a severe flash area caused by entrained CO₂ near the inlet area. Owing to the high steam generation rate in this area, the overall flash steam generation rate of the flash chamber also increased.

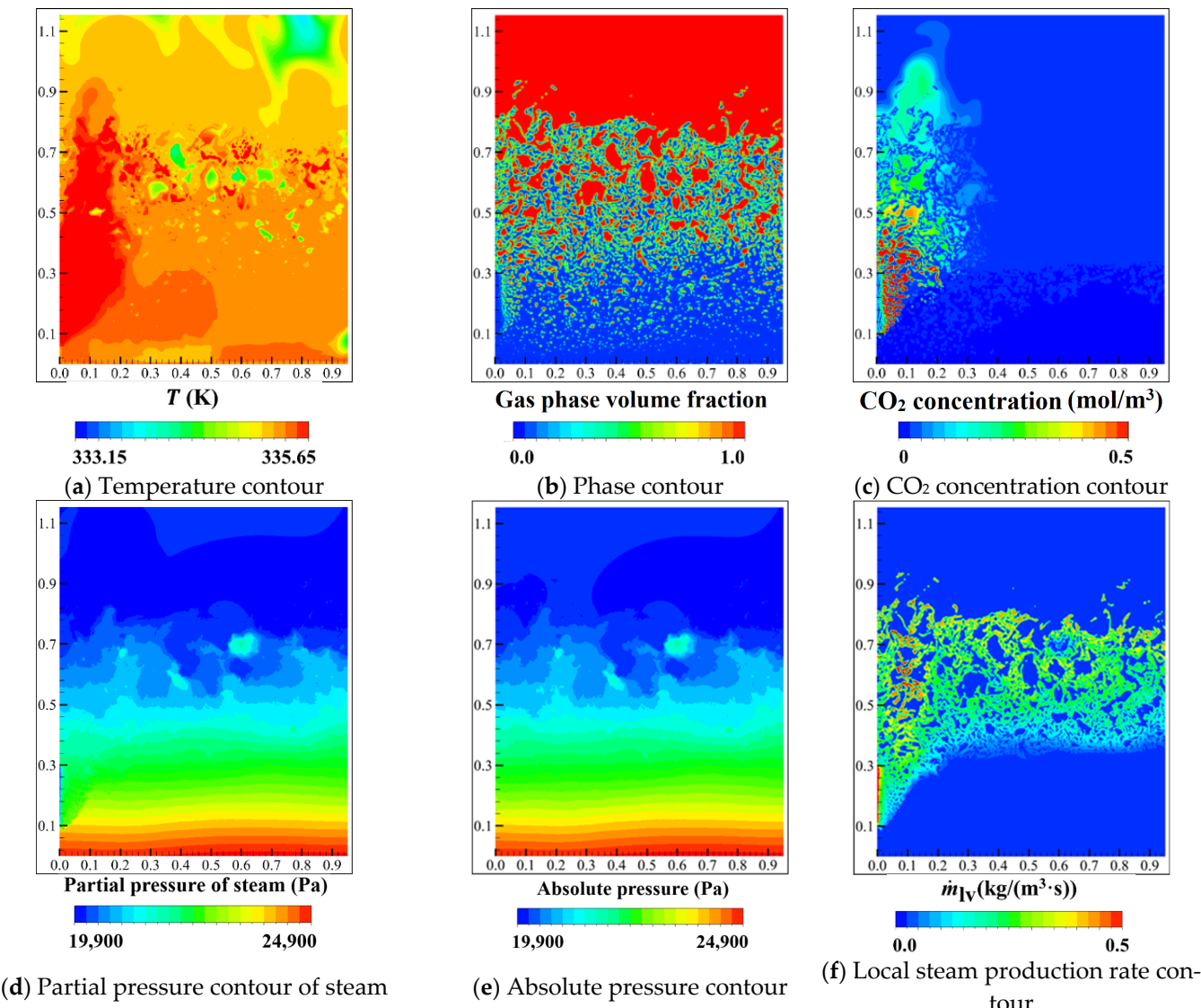


Figure 7. Characteristic distribution of the flash chamber for the 1 vol% entrained CO₂ volume fraction.

The phase distribution and local CO₂ release rate distribution are shown in Figures 8 and 9. Under the condition of a higher inlet entrained CO₂ volume fraction, the phase-change process in the intense flash area is slightly changed because the increase in the inlet flow rate of entrained CO₂ increased local CO₂ concentration; however, the increase in the inlet flow rate also intensified the bubble uplift process, thus narrowing the area of the intense flashing area around the inlet. In general, the more inlet-entrained CO₂ shrank the

region of the intense flash area, but increasing the intensity of the phase transition, and had little effect on the gas–liquid distribution.

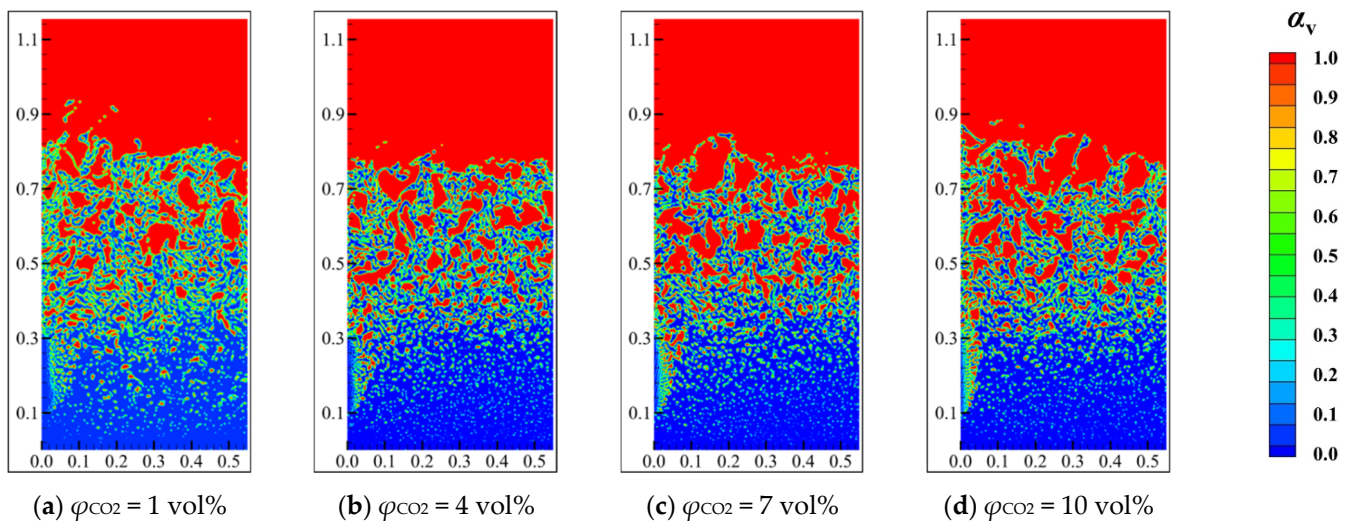


Figure 8. Gas- and liquid-phase distribution for different entrained CO_2 volume fractions.

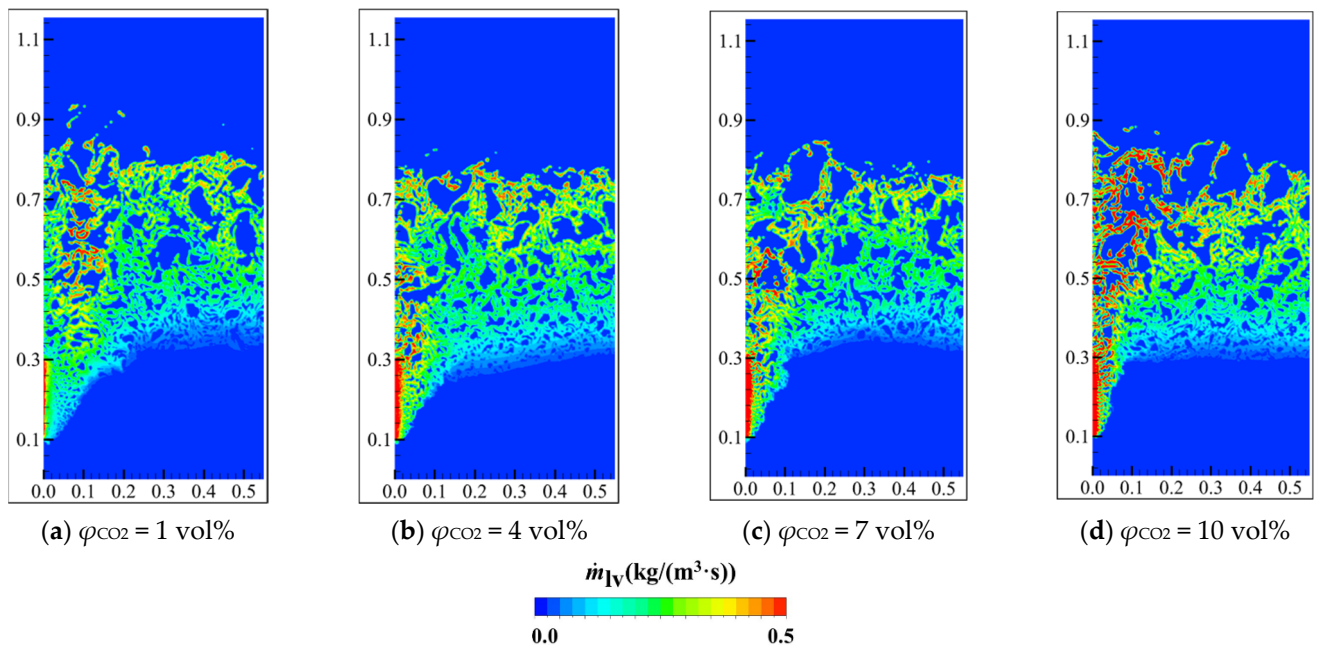


Figure 9. Local CO_2 release rate distribution for different entrained CO_2 volume fractions.

3.3. Effect of Dissolved CO_2 Concentration on Flash Performance

Figure 10 shows the steam and CO_2 generation rates after stabilization for different dissolved CO_2 mass concentrations. Compared with pure water, the steam generation rate increased by 2.1%, 4.8%, 6.2%, and 7.5%, corresponding to dissolved CO_2 mass concentrations of 0.0661%, 0.1004%, 0.1348%, and 0.1688% (g/g), respectively. The ratio of the CO_2 release rate to the steam generation rate was 0.011%, 0.017%, 0.024%, and 0.030%, respectively. The steam generation rate and CO_2 release rate both increased linearly with increasing dissolved CO_2 mass concentration. Under different working conditions, the interfacial release CO_2 rate was approximately 1.8 times higher than the supersaturated dissolution release CO_2 rate.

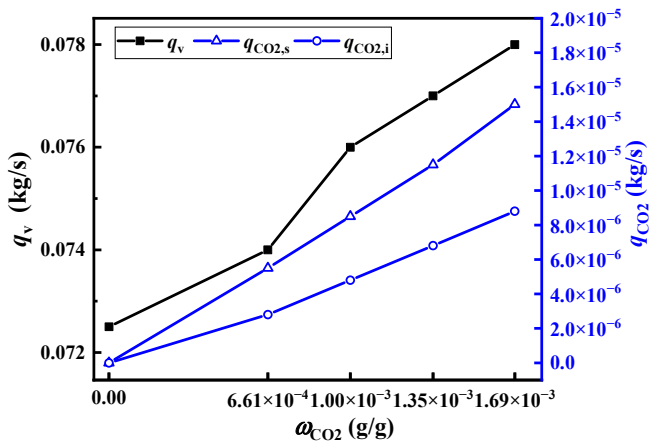


Figure 10. Variation in the steam generation rate and CO₂ release rate of different dissolved CO₂ mass fraction values.

Figure 11 presents the distributions of the CO₂ concentration, CO₂ interfacial release rate, CO₂ supersaturated release rate, and local steam generation rate. Figure 11a shows that the volume fraction of CO₂ in gas in the entire flash space is small, which has little effect on the partial pressure of water vapor and did not cause a significant effect on the rate of vapor generation. In addition, as shown in Figure 11b–d, the release rate of CO₂ was three to four orders of magnitude lower than the steam generation rate, thus the flow field disturbance by the release of CO₂ is not significant.

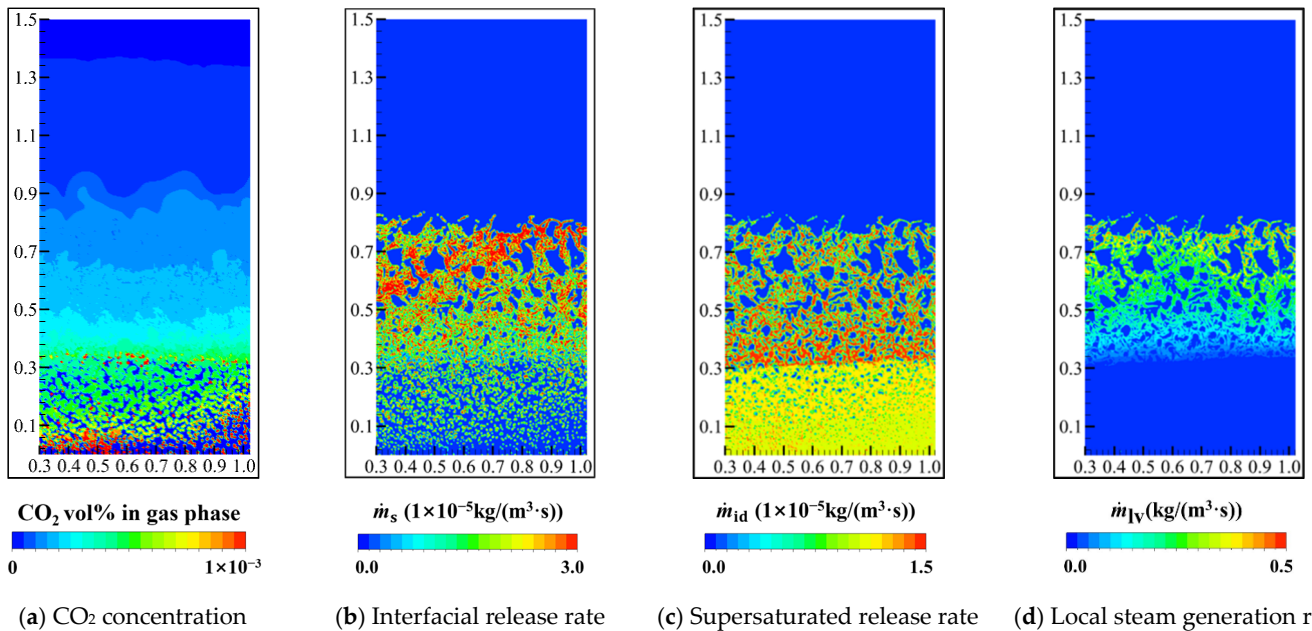


Figure 11. Distribution of CO₂ release and steam generation.

The phase distributions for the different dissolved CO₂ mass fractions are shown in Figure 12. The phase distributions for different cases were slightly different owing to the release of CO₂. Compared with the pure-water flashing condition, the intense flashing area in the flashing chamber increased, but the change was small. Compared with the flash evaporation process of pure water without CO₂, the release of dissolved CO₂ causes a low local partial pressure of water vapor in the bottom water body, resulting in denser bubbles of the mixed components of water vapor and CO₂ during slow flash evaporation. This causes the steam generation rate to increase slightly and leads to the junction between the severe flash region and slow flash region being not very obvious, especially for a

high dissolved CO₂ concentration. The liquid height showed little increase, and a larger liquid–gas interface was produced, which also led to an increase in steam generation.

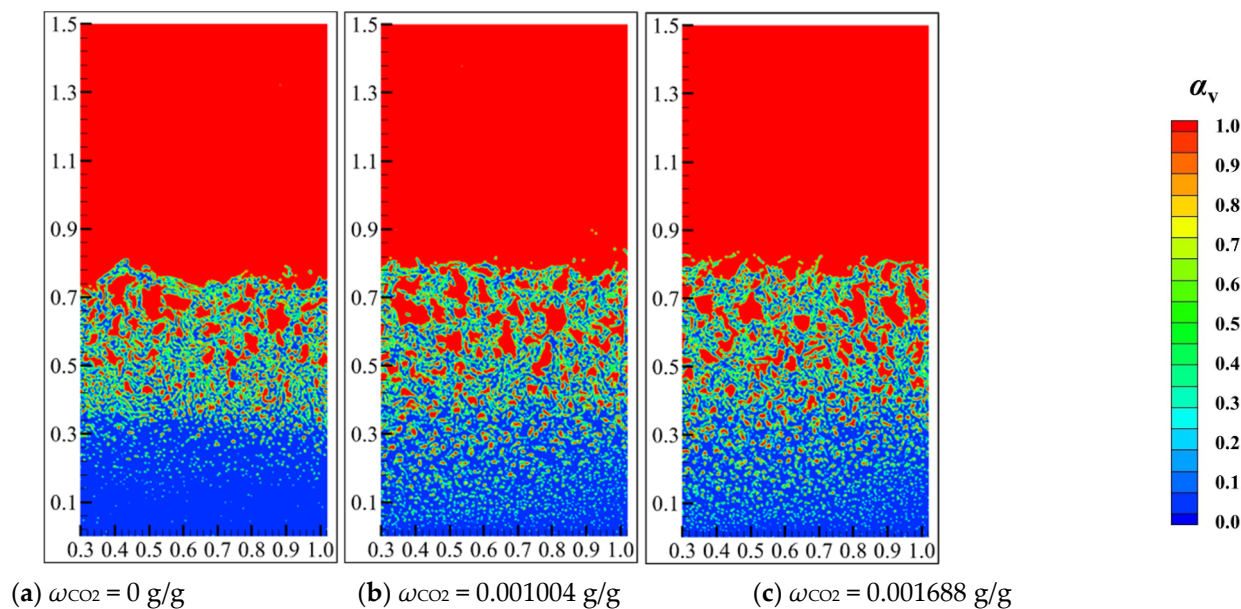


Figure 12. Phase distribution for different dissolved CO₂ mass fractions.

4. Conclusions

In this study, a multiphase, multicomponent, and pressure-driven Lee phase-change model was constructed to numerically study water flash evaporation with non-condensing CO₂. The numerical model can effectively predict the flash evaporation process, and an intense flash evaporation area around the inlet and a reduction in the partial pressure of vapor caused by the release of CO₂ in the flash chamber were observed using this model, which makes the presence of CO₂ enhance the intensity of vapor generation. Overall, the increase ratio of steam generation can reach 4.8–20% and 2.1–7.5% for a 1–10% volume concentration of dissolved CO₂ and 0.0661–0.1688% mass concentration of entrained CO₂, respectively.

Author Contributions: Conceptualization, Y.S.; Methodology, B.L. (Bingrui Li) and B.L. (Bingxi Li); Software, X.W.; Validation, X.W.; Data curation, B.L. (Bingrui Li); Writing—review & editing, W.W.; Funding acquisition, W.W. All authors have read and agreed to the published version of the manuscript.

Funding: This study is supported by the National Natural Science Foundation of China (52106082), China Postdoctoral Science Special Foundation (2022T150160), and Heilongjiang Provincial Science Foundation (LH2022E064).

Institutional Review Board Statement: Not applicable.

Informed Consent Statement: Not applicable.

Data Availability Statement: The data presented in this study are available on request from the corresponding author.

Conflicts of Interest: The authors declare no conflict of interest.

Nomenclature

A	Interface area (m^2)
c	Time relaxation parameters (s^{-1})
c_p	Specific heat ($\text{J}/(\text{kg}\cdot\text{K})$)
E	Internal energy (J/kg)
F_{CSF}	Volume force caused by surface tension ($\text{kg}/(\text{m}^2\cdot\text{s}^2)$)
g	Gravitational acceleration vector (m/s^2)
h	Initial water level height (m)
J	Diffusion flux
\dot{m}_i	Source terms of mass transfer ($\text{kg}/(\text{m}^3\cdot\text{s})$)
k	Turbulent kinetic energy (m^2/s^2)
p	Pressure (Pa)
$p_{\text{out},l}$	Pressure of liquid outlet (Pa)
$p_{\text{out},v}$	Pressure of vapor outlet (Pa)
$q_{\text{m},v}$	Mass rate of vapor generation (kg/s)
r	Latent heat (J/kg)
\dot{S}_i	Source terms of energy (W/m^3)
t	Time (s)
T	Temperature (K)
T_{in}	Inlet temperature (K)
T_{sat}	Saturation temperature (K)
v	Velocity vector (m/s)
Y_i	Mass fraction of species i
Greek letters	
α_i	Volume fraction of phase i
ε	Turbulent dissipation rate (m^2/s^3)
κ	Curvature of the interface (m^{-1})
λ	Thermal conductivity ($\text{W}/(\text{m}\cdot\text{K})$)
μ	Dynamic viscosity ($\text{kg}/(\text{m}\cdot\text{s})$)
ρ	Density (kg/m^3)
σ	Surface tension coefficient (kg/s^2)
φ	Volume concentrations of CO_2 carried by water
ω	Mass concentrations of dissolved CO_2 in water
Subscripts	
aq	Dissolved in water
CO_2	Carbon dioxide
g	Gas
id	Interfacial diffusion
l	Liquid
lv	Liquid to vapor
s	Supersaturated released
v	Vapor
w	Water

References

- Zou, L.; Zhang, X.; Zheng, Q. Research progress on preparation of binary ice by vacuum flash evaporation: A review. *Int. J. Refrig.* **2021**, *121*, 72–85. [[CrossRef](#)]
- Mansour, A.; Müller, N. A review of flash evaporation phenomena and resulting shock waves. *Exp. Therm. Fluid Sci.* **2019**, *107*, 146–168. [[CrossRef](#)]
- Maria Antony Raj, M.; Kalidasa Murugavel, K.; Rajaseenivasan, T.; Srithar, K. A review on flash evaporation desalination. *Desalination Water Treat.* **2016**, *57*, 13462–13471. [[CrossRef](#)]
- Guo, Y.L.; Yan, J.J.; Chong, D.T.; Liu, J.P. Experimental investigation on some key variables during pool water flash evaporation. *AIP Conf. Proc.* **2010**, *1207*, 380–385. [[CrossRef](#)]
- Wu, H.; Liu, W.; Li, X.; Chen, F.; Yang, L. Experimental Study on Flash Evaporation under Low-pressure Conditions. *J. Appl. Sci. Eng.* **2019**, *22*, 213–220. [[CrossRef](#)]
- Zhang, Y.; Wang, J.; Yan, J.; Chong, D.; Liu, J. Experimental study on energy transformation and separation characteristic of circulatory flash evaporation. *Int. J. Heat Mass Transf.* **2016**, *99*, 862–871. [[CrossRef](#)]

7. Ni, P.; Wen, Z.; Su, F. Influence of different air inflow rates on low-pressure flash evaporation from a water pool. *Int. J. Therm. Sci.* **2022**, *171*, 107234. [[CrossRef](#)]
8. Chi, J.; Shen, S.; Mu, X. Experimental study on thermal characteristics of pure water flashing evaporation from thin-liquid film. *Appl. Therm. Eng.* **2023**, *233*, 121075. [[CrossRef](#)]
9. Lior, N.; Nishiyama, E. Some experiments on flash evaporation enhancement by electrolytically generated bubbles. *Desalination* **1995**, *100*, 71–76. [[CrossRef](#)]
10. Tian, S.; Gu, Y.; Ju, S.; Xu, L.; Zhang, L.; Zhang, L.; YuWen, C. Study on heat transfer process of microwave flash evaporation using water as medium. *Int. J. Heat Mass Transf.* **2021**, *166*, 120795. [[CrossRef](#)]
11. Wang, C.; Xu, R.; Chen, X.; Jiang, P.; Liu, B. Study on water flash evaporation under reduced pressure. *Int. J. Heat Mass Transf.* **2019**, *131*, 31–40. [[CrossRef](#)]
12. Zhang, D.; Chong, D.; Yan, J.; Zhao, B. Experimental study on static flash evaporation of aqueous NaCl solution at different flash speed: Heat transfer characteristics. *Int. J. Heat Mass Transf.* **2013**, *65*, 584–591. [[CrossRef](#)]
13. Xie, J.; Song, J.; Ding, C. Experimental and numerical investigation of evaporation and the dependence of flash points on the ignition spots at an open-cup method. *Thermochim. Acta* **2023**, *719*, 179417. [[CrossRef](#)]
14. Cheng, W.-l.; Chen, H.; Hu, L.; Zhang, W.-w. Effect of droplet flash evaporation on vacuum flash evaporation cooling: Modeling. *Int. J. Heat Mass Transf.* **2015**, *84*, 149–157. [[CrossRef](#)]
15. Gao, W.Z.; Sun, W.Z.; Anderson, K.; Cheng, Y.P.; Li, A. Investigation on temperature distribution of flash evaporation of LiCl droplets released into vacuum. *Int. J. Heat Mass Transf.* **2014**, *74*, 414–420. [[CrossRef](#)]
16. Ji, C.; Wang, N.; Liu, Z. Three-dimensional simulation of flash evaporation of non-uniform spray in saturated vapor environment. *Heat Mass Transf.* **2020**, *56*, 3289–3301. [[CrossRef](#)]
17. Jin, W.X.; Low, S.C. Investigation of single-phase flow patterns in a model flash evaporation chamber using PIV measurement and numerical simulation. *Desalination* **2002**, *150*, 51–63. [[CrossRef](#)]
18. Wang, C.; Xu, R.; Song, Y.; Jiang, P. Study on water droplet flash evaporation in vacuum spray cooling. *Int. J. Heat Mass Transf.* **2017**, *112*, 279–288. [[CrossRef](#)]
19. Drożyński, Z. Steam condensation analysis in a power plant condenser. *Arch. Thermodyn.* **2018**, *39*, 3–32. [[CrossRef](#)]
20. Dilli, B.; Abraham, R.; Venkata Ramana Murthy, M. Experimental study on the vacuum load of low-temperature thermal desalination plant. *Desalination Water Treat.* **2016**, *57*, 26830–26844. [[CrossRef](#)]
21. Gentner, K.; Gregorzewski, A.; Seifert, A. The effects and limitations issued by non-condensable gases in sea water distillers. *Desalination* **1993**, *93*, 207–234. [[CrossRef](#)]
22. Kotcioglu, I.; Uyarel, A.Y.; Kaygusuz, K.; Gullapoglu, S.; Dincer, I. An approach to heat and mass transfer analysis during film condensation inside a vertical tube. *Int. Commun. Heat Mass Transf.* **1993**, *20*, 265–277. [[CrossRef](#)]
23. Sun, F.; Yao, Y.; Li, X. The heat and mass transfer characteristics of superheated steam coupled with non-condensing gases in horizontal wells with multi-point injection technique. *Energy* **2018**, *143*, 995–1005. [[CrossRef](#)]
24. Zhang, A.; Wang, Y.; Sun, D.; Yu, S.; Yu, B.; Li, Y. Development of a VOF+LS+SPP method based on FLUENT for simulating bubble behaviors in the electric field. *Numer. Heat Transf. Part B Fundam.* **2017**, *71*, 186–201. [[CrossRef](#)]
25. Hirt, C.W.; Nichols, B.D. Volume of fluid (VOF) method for the dynamics of free boundaries. *J. Comput. Phys.* **1981**, *39*, 201–225. [[CrossRef](#)]
26. Fluent, A. *Ansys Fluent Theory Guide*; ANSYS Inc.: Canonsburg, PA, USA, 2011; Volume 15317, pp. 724–746.
27. Pan, Z.; Weibel, J.A.; Garimella, S.V. Spurious Current Suppression in VOF-CSF Simulation of Slug Flow through Small Channels. *Numer. Heat Transf. Part A Appl.* **2015**, *67*, 1–12. [[CrossRef](#)]
28. Tsui, Y.-Y.; Liu, C.-Y.; Lin, S.-W. Coupled level-set and volume-of-fluid method for two-phase flow calculations. *Numer. Heat Transf. Part B Fundam.* **2017**, *71*, 173–185. [[CrossRef](#)]
29. Banerjee, R. A Numerical Study of Combined Heat and Mass Transfer in an Inclined Channel Using the VOF Multiphase Model. *Numer. Heat Transf. Part A Appl.* **2007**, *52*, 163–183. [[CrossRef](#)]
30. Zhang, Q.; Wang, X.; Ruan, W.; Chen, Q.; Liu, Z. Performance study of finned tube evaporative air cooler based on experiment and numerical simulation. *Numer. Heat Transf. Part A Appl.* **2018**, *74*, 1154–1174. [[CrossRef](#)]
31. Li, H.; Wilhelmsen, Ø.; Lv, Y.; Wang, W.; Yan, J. Viscosities, thermal conductivities and diffusion coefficients of CO₂ mixtures: Review of experimental data and theoretical models. *Int. J. Greenh. Gas Control* **2011**, *5*, 1119–1139. [[CrossRef](#)]
32. Massman, W.J. A review of the molecular diffusivities of H₂O, CO₂, CH₄, CO, O₃, SO₂, NH₃, N₂O, NO, and NO₂ in air, O₂ and N₂ near STP. *Atmos. Environ.* **1998**, *32*, 1111–1127. [[CrossRef](#)]
33. Wang, W.; Li, B.; Tan, Y.; Li, B.; Shuai, Y. Multi-objective optimal design of NACA airfoil fin PCHE recuperator for micro-gas turbine systems. *Appl. Therm. Eng.* **2022**, *204*, 117864. [[CrossRef](#)]
34. Banerjee, R.; Isaac, K.M. Evaluation of Turbulence Closure Schemes for Stratified Two Phase Flow. In Proceedings of the ASME 2003 International Mechanical Engineering Congress and Exposition, Washington, DC, USA, 15–21 November 2003; Volume 259.
35. Zhou, N.; Chen, F.; Cao, Y.; Chen, M.; Wang, Y. Experimental investigation on the performance of a water spray cooling system. *Appl. Therm. Eng.* **2017**, *112*, 1117–1128. [[CrossRef](#)]
36. Wang, W.; Shuai, Y.; Ding, L.; Li, B.; Sundén, B. Investigation of complex flow and heat transfer mechanism in multi-tube heat exchanger with different arrangement corrugated tube. *Int. J. Therm. Sci.* **2021**, *167*, 107010. [[CrossRef](#)]

37. Wang, W.; Shuai, Y.; Li, B.; Li, B.; Lee, K.-S. Enhanced heat transfer performance for multi-tube heat exchangers with various tube arrangements. *Int. J. Heat Mass Transf.* **2021**, *168*, 120905. [[CrossRef](#)]
38. Ding, S.-T.; Luo, B.; Li, G. A volume of fluid based method for vapor-liquid phase change simulation with numerical oscillation suppression. *Int. J. Heat Mass Transf.* **2017**, *110*, 348–359. [[CrossRef](#)]
39. Vreme, A.; Pouliquen, B.; Nadal, F.; Liger-Belair, G. Does shaking increase the pressure inside a bottle of champagne? *J. Colloid Interface Sci.* **2015**, *439*, 42–53. [[CrossRef](#)] [[PubMed](#)]
40. Zhang, Y.; Wang, J.; Liu, J.; Chong, D.; Zhang, W.; Yan, J. Experimental study on heat transfer characteristics of circulatory flash evaporation. *Int. J. Heat Mass Transf.* **2013**, *67*, 836–842. [[CrossRef](#)]

Disclaimer/Publisher’s Note: The statements, opinions and data contained in all publications are solely those of the individual author(s) and contributor(s) and not of MDPI and/or the editor(s). MDPI and/or the editor(s) disclaim responsibility for any injury to people or property resulting from any ideas, methods, instructions or products referred to in the content.